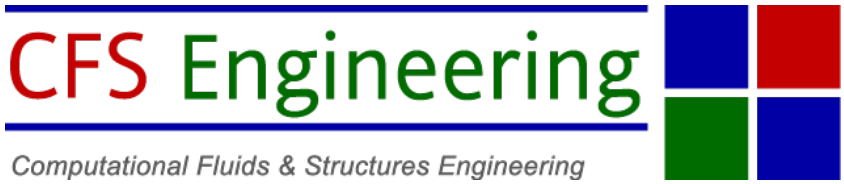

INTERNSHIP REPORT

June 9th 2025 – September 26th 2025

A Study of Thermo-Chemical Non-Equilibrium and Multi-Temperature Models in Hypersonic Re-entry Vehicles Using Computational Fluid Dynamics

APPLIED TO THE ELECTRE TEST CASE

September 25, 2025

Author:

Justine Brun

Supervised by:

Jan Vos

Contents

Abstract

This report presents a numerical study of thermo-chemical non-equilibrium and multi-temperature modeling effects in hypersonic re-entry flows, focusing on the ELECTRE flight experiment conducted by the ONERA. The objective is to simulate and analyze the key physico-chemical processes occurring in the shock layer around a re-entry vehicle, using the NSMB (Navier–Stokes Multi-Block) solver with multi-species, multi-temperature air models.

Simulations were performed using an axi-symmetric configuration, using an 11-species air model with varying thermo-chemical kinetics. The results are compared with reference flight data and other computational models to assess the accuracy of different modeling strategies. Emphasis is placed on predicting stagnation-line temperature profiles, number density distributions, surface heat flux and the influence of different thermo-chemical catalyticity models.

This work highlights the challenges of simulating hypersonic flow in transitional regimes. The ELECTRE case provides a valuable validation benchmark for high-fidelity CFD tools used in atmospheric entry analysis.

List of Figures

List of Tables

1 Introduction

The accurate prediction of hypersonic flow phenomena during atmospheric re-entry is crucial for the design and safe operation of spacecraft. One key challenge lies in modeling the complex thermo-chemical processes that govern the behavior of the shock layer formed around the vehicle.

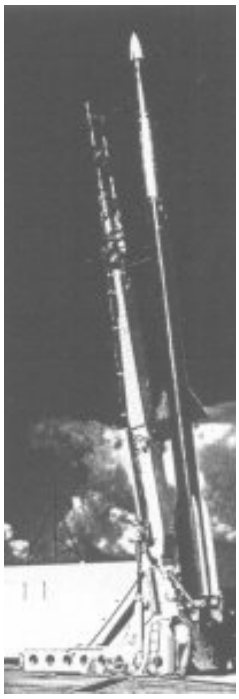

Figure 1: Launch of ELECTRE mission

Hypersonic flows at Mach numbers on the order of 20, typical of re-entry trajectories, result in extreme aerodynamic heating and strong shock waves. These conditions cause the atmospheric gas to dissociate and partially ionize in the shock-compressed layer near the vehicle surface. The intensity and nature of these physico-chemical processes vary significantly with altitude.

To validate computational models that aim to capture these non-equilibrium phenomena, reliable flight data is essential. This study focuses on the simulation of flow around the ELECTRE reentry vehicle, developed by the Office National d'Études et de Recherches Aérospatiales (ONERA), for which extensive experimental and numerical datasets are available.

The numerical methodology employed involves solving the Navier–Stokes equations coupled with detailed thermo-chemical non-equilibrium models and mutil-temperature models. Several chemical kinetic models are tested for their ability to reproduce key aerothermal features, particularly along the stagnation region.

Objectives include validating the simulations against reference data, analyzing flow properties such as heat flux and temperatures, and assessing the predictive reliability of different thermochemical models for hypersonic reentry conditions.

2 ELECTRE flight experiments

The ELECTRE vehicle, developed by ONERA as part of the European Hermes program, has been widely adopted as a reference case for validating CFD codes involving thermo-chemical non-equilibrium effects [2]-[7]. Two flight experiments were conducted in the early 1970s, with the first mission in 1971 yielding in-flight aerothermal measurements during atmospheric reentry.

The reentry phase of the first flight lasted approximately 10 seconds, as the capsule descended from 60 to 20 km altitude at velocities between 4200 and 3800 m/s (Mach $\approx$ 13). Ten thermocouples placed inside the vehicle recorded internal wall temperatures, from which surface heat flux could be inferred [2]. These measurements have since served as key benchmarks for

validating numerical models in the high-enthalpy hypersonic regime.

Geometrically, the ELECTRE capsule features a spherical nose of radius 0.175 m connected to a 4.6° cone, with an overall length of 2 m. The vehicle is constructed with a metallic skin : copper on the forebody and titanium on the cone. It has a mass of approximately 130 kg.

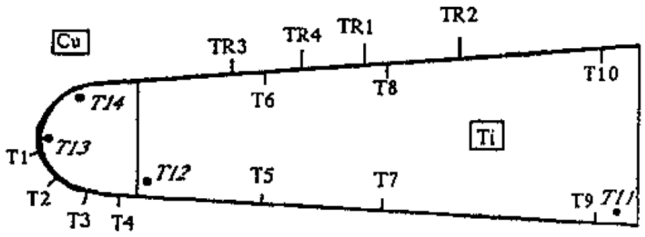

Figure 2: ELECTRE scheme with thermocouple locations

The availability of both detailed flight data and supporting numerical studies makes ELECTRE an ideal case for evaluating heat flux prediction and shock-layer modeling. This work simulates the configuration at $t = 293$ s using the CFD solver NSMB, with a focus on assessing the impact of multi-temperature models on the computed flowfield.

3 Simulation configuration

3.1 Geometry & meshing

The ELECTRE vehicle was modeled using an axisymmetric approximation, consistent with its nominally symmetric geometry. Although a small angle of attack was present during the flight, it is considered negligible for the purposes of this study. These simplifications reduce computational cost while preserving the essential physical features of the flow. A multi-block, structured mesh was used to discretize the flow domain. The mesh was designed to resolve the bow shock and the boundary layer with sufficient accuracy.

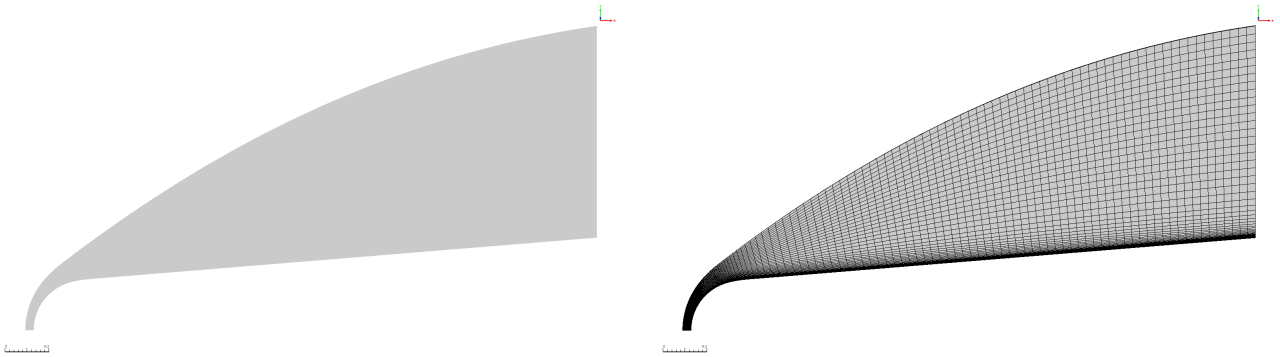

(a) Geometry (b) Computational mesh

Figure 3: Geometric configuration for the simulation of the ELECTRE vehicle

Figure 3a shows the axi-symmetic modeling of the ELECTRE geometry, while Figure 3b provides an overview of the computational mesh used in the simulations.

3.2 The NSMB solver

All CFD computations in this study were performed using the Navier–Stokes Multi Block (NSMB) solver, developed by a consortium of universities and industry partners [1]. NSMB is a parallelized, cell-centered finite volume solver designed for compressible flows on structured multi-block grids.

The code supports both explicit and implicit time integration schemes, with second- and fourth-order central discretizations (with artificial dissipation), as well as several upwind schemes up to fifth order. Turbulence modeling includes validated RANS models (up to 5 equations), LES, hybrid RANS–LES, and transition models.

NSMB was originally developed with hypersonic applications in mind, such as atmospheric re-entry. It includes various levels of chemical modeling for air, CO_2, and N_2, with available air models incorporating 5, 7, 11, or 13 species. Non-equilibrium models include those by Park (1989–2001), Gardiner, and Dunn–Kang, using equilibrium constants computed from polynomial fits (further details available in [1]).

Thermo-chemical non-equilibrium is modeled via the Landau–Teller theory for translational – vibrational energy exchange, with Millikan–White relaxation times. Transport coefficients are computed using the Blottner model or the Gupta-Yos model. Both inviscid and viscous flows (laminar and turbulent) are supported. Wall boundary conditions allow for super- and partially catalytic surfaces.

NSMB has been employed extensively in various European projects, demonstrating its versatility and robustness across a range of aerodynamic applications.

3.3 Numerical parameters

The simulations were carried out using the following numerical parameters. A total of 15 000 time steps (`NSTEPS`) were performed to advance the solution toward convergence. The Courant–Friedrichs–Lewy (CFL) number was initially set to 0.1, and gradually increased by a factor of 1.01 to a maximum of 5.0, ensuring numerical stability and convergence efficiency. An implicit time integration scheme was employed, allowing for larger time steps and improved stability in capturing the flow features of hypersonic regimes.

A central differencing scheme was used for spatial discretization in combination with a standard artificial dissipation model.

To accurately capture shock waves and steep gradients, an `automatic` shock adaptation was performed in four successive stages. After completing the adaptation, the simulation was continued for an additional 2 000 steps to reach the final steady-state solution.

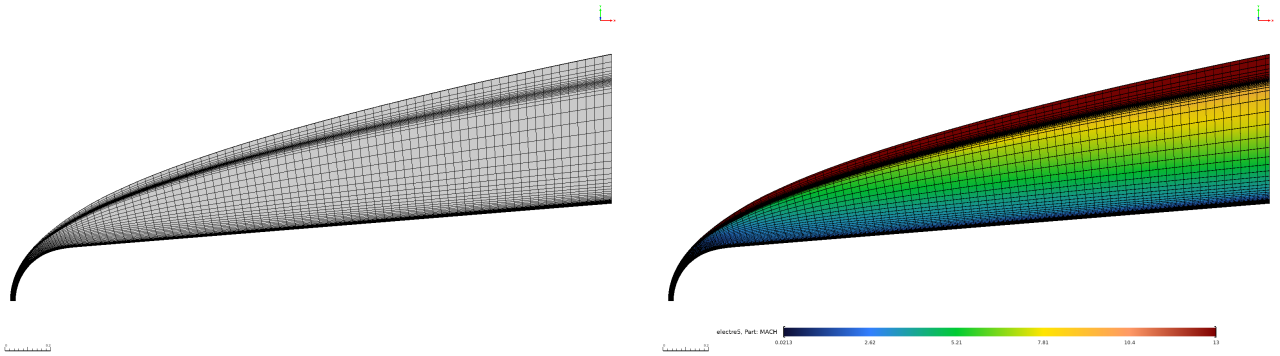

(a) Mesh after shock adaptation (b) Mesh refinement interface with Mach number

Figure 4: Shock adaptation process

Figure 4 illustrates the effect of the shock adaptation process on the computational mesh. Figure 3b shows the initial mesh before adaptation, while Figure 4a presents the refined mesh and grid bunching after shock adaptation. The corresponding Mach number distribution is shown in Figure 4b.

3.4 Flow model

The atmosphere is considered as a continuum since the Knudsen number is less than 0.01. Specifically :

$$\mathrm{Kn} = \frac{\lambda}{L} \approx 0.0007 \quad \text{with} \quad \begin{cases} \lambda = 0.119 \cdot 10^{-3}\,\mathrm{m}\text{: mean free path} \\ L = R_n = 0.175\,\mathrm{m}\text{: capsule's characteristic length} \end{cases}$$

The simulations were conducted under the assumption of steady-state conditions. A laminar flow model was employed, appropriate for the flow regime under consideration. Viscous effects were represented using Gupta-Yos-Thompson's model to accurately capture thermal conductivity behavior.

3.5 Kinetic model

The assumption of a quiescent, chemically frozen atmosphere at inflow is applied. The following assumptions are made at the inflow boundary:

- The air is considered a reacting gas mixture, composed of multiple species, including both neutral and ionized components.
- The inflow temperature and pressure are such that only the major neutral species (N_2, O_2) are present in significant amounts, while minor species and ionized components are initialized at trace concentrations.
- A specific air model with 7 or 11 species is selected depending on the study carried out.

3.5.1 Chemical species

The chemical species considered are summarized in Table 1.

7 species	11 species
Molecular nitrogen (N_2)	Molecular nitrogen (N_2)
Molecular oxygen (O_2)	Molecular oxygen (O_2)
Nitric oxide (NO)	Nitric oxide (NO)
Atomic nitrogen (N)	Atomic nitrogen (N)
Atomic oxygen (O)	Atomic oxygen (O)
Electrons (e^-)	Ionized nitric oxide (NO^+)
Ionized species	Ionized molecular nitrogen (N_2^+)
	Ionized molecular oxygen (O_2^+)
	Atomic nitrogen ion (N^+)
	Atomic oxygen ion (O^+)
	Electron (e^-)

Table 1: Chemical species considered in the 7- and 11-species air models

3.5.2 Chemical reactions

In this work, we will primarily focus on the 11-species air model. Accordingly, the following reactions, including dissociation, recombination, ionization and charge exchange processes, are considered (as reported in [8]):

$$N_2 + M \rightleftharpoons 2N + M \quad (1)$$
$$O_2 + M \rightleftharpoons 2O + M \quad (2)$$
$$NO + M \rightleftharpoons N + O + M \quad (3)$$
$$N_2 + O \rightleftharpoons NO + N \quad (4)$$
$$NO + O \rightleftharpoons O_2 + N \quad (5)$$
$$N + O \rightleftharpoons NO^+ + e^- \quad (6)$$
$$N + N \rightleftharpoons N_2^+ + e^- \quad (7)$$
$$O + O \rightleftharpoons O_2^+ + e^- \quad (8)$$
$$N + e^- \rightleftharpoons N^+ + 2e^- \quad (9)$$
$$O + e^- \rightleftharpoons O^+ + 2e^- \quad (10)$$
$$N_2 + O_2^+ \rightleftharpoons N_2^+ + O_2 \quad (11)$$
$$NO^+ + N \rightleftharpoons O^+ + N_2 \quad (12)$$
$$O^+ + N_2 \rightleftharpoons N_2^+ + O \quad (19)$$
$$NO^+ + O \rightleftharpoons N^+ + O_2 \quad (13)$$
$$NO^+ + O_2 \rightleftharpoons NO + O_2^+ \quad (14)$$
$$NO^+ + N \rightleftharpoons N_2^+ + O \quad (15)$$
$$O_2^+ + N \rightleftharpoons N^+ + O_2 \quad (16)$$
$$O^+ + NO \rightleftharpoons NO^+ + O \quad (17)$$
$$NO^+ + O \rightleftharpoons O_2^+ + N \quad (18)$$

where M represents any species acting as a third body to conserve energy and momentum.

3.5.3 Mass fractions

We assume the atmosphere's air has the composition presented in Table 2.

Species	Mass fraction
N_2	0.76536
O_2	0.23464
N	1×10^{-12}
NO	1×10^{-12}
O	1×10^{-12}
NO^+	1×10^{-12}
N_2^+	1×10^{-12}
O_2^+	1×10^{-12}
N^+	1×10^{-12}
O^+	1×10^{-12}
e^-	1×10^{-12}

Table 2: Initial mass fractions at the inflow boundary

3.6 Thermo-chemical models

The kinetic model employed in this study accounts for thermo-chemical non-equilibrium effects, typical of hypersonic flow environments. These effects arise at high speeds and altitudes when the characteristic flow time around a hypersonic vehicle is comparable to or shorter than the time required for molecular collisions to restore equilibrium. Chemical non-equilibrium effects are captured using `gas model 4`, while thermo-chemical non-equilibrium, where both chemical kinetics and internal energy mode relaxation are treated in a coupled manner, is modeled using `gas model 5`. Electronic non-equilibrium is modeled using `gas model 6`.

To model the vibrational relaxation behavior of diatomic molecules initially, Millikan-White's empirical model was considered for the vibrational relaxation time.

3.7 Boundary conditions

The inflow boundary conditions correspond to the free-stream experimental data reported in [3] at $t = 293\,\mathrm{s}$. The wall temperature is fixed at $T_{\mathrm{wall}} = 343\,\mathrm{K}$. The surface is initially considered non-catalytic. Ablation is not considered here.

3.8 Conditions for the ELECTRE test case

Table 3 presents the initial data for the numerical modeling as described in [2] and [3]. All input files were initialized using these conditions.

Flight time (s)	Altitude (km)	ρ_∞ (kg/m^3)	$\mathbf{T}_\infty$ (K)	$\mathbf{T}_{\mathbf{wall}}$ (K)	$\mathbf{u}_\infty$ (m/s)
293	53.3	$6.963 \cdot 10^{-4}$	265	343	4230

Table 3: Flow and wall conditions for the ELECTRE simulation at $t = 293$ s

It should be noted that the reference curves used from the literature used later on in this report were not available in electronic format and were therefore digitized manually. As a result, some uncertainty and limited precision should be considered when interpreting these comparisons.

4 Numerical simulation results

The flow field is simulated using NSMB with different thermo-chemical and catalyticity models. The results are primarily compared against the recent study by Kim [3], which provides detailed reference data for multi-temperature modeling. While our focus is on this latest work, it is worth noting that the predictions from Kim [3] are generally consistent with earlier investigations [4, 5, 6, 7], which also explored the influence of non-equilibrium effects and chemical kinetics on temperature distributions, surface heat flux, and ionization behavior.

4.1 Flow property contours along the capsule skin

The results presented in Figure 5 were obtained from flow simulations using a 7-species air model based on Park's 1989 chemical non-equilibrium model. Figure 5c highlights the strong shockwave that forms ahead of the capsule's forebody. The boundary layer remains relatively thin due to the intermediate flight speed of the ELECTRE vehicle.

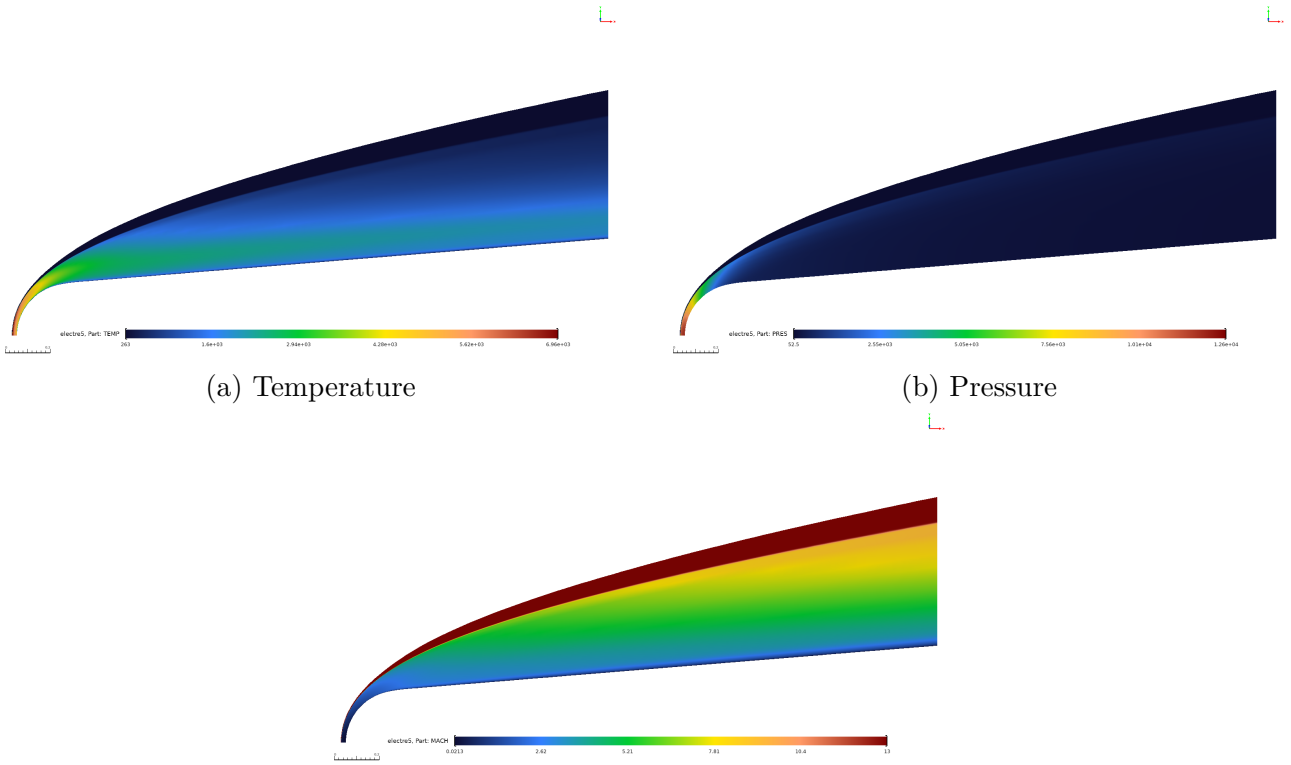

(a) Temperature

(b) Pressure

(c) Mach number

Figure 5: Flow property contours obtained with Park's 1989 non-equilibrium chemistry model for the 7-species air and the Blottner-Eucken viscosity models

Similar contours are observed for other configuration models, with only minor variations in the values and slight differences in the shock layer thickness.

4.2 Temperature distributions along the stagnation streamline

Figure 6 presents the translational, vibrational, and electron-electronic temperatures along the stagnation line.

For the translational temperature profiles (Fig. 6a), all models exhibit a steep rise from the free-stream to the post-shock region, reaching values between 6000 and 6500 K near the stagnation point. The differences among the 2-T, 3-T, Millikan–White, Millikan–White with Parks correction (MWP), and Millikan–White–Kim (MWKim) models remain small in this region, indicating that the translational temperature is only weakly influenced by the degree of non-equilibrium modeling. Notably, the shock region is well captured by all models, with the exception of the 1-T model, which predicts a lower shock temperature compared to the

others but an agreeing shock position. Furthermore, both non-catalytic and fully catalytic wall conditions yield similar post-shock plateau temperatures. Comparison with Kim [3] shows good agreement: both the slope through the shock and the stagnation-point plateau are similar, although Kim's results predict a slightly upstream shock front and a lower stagnation point temperature.

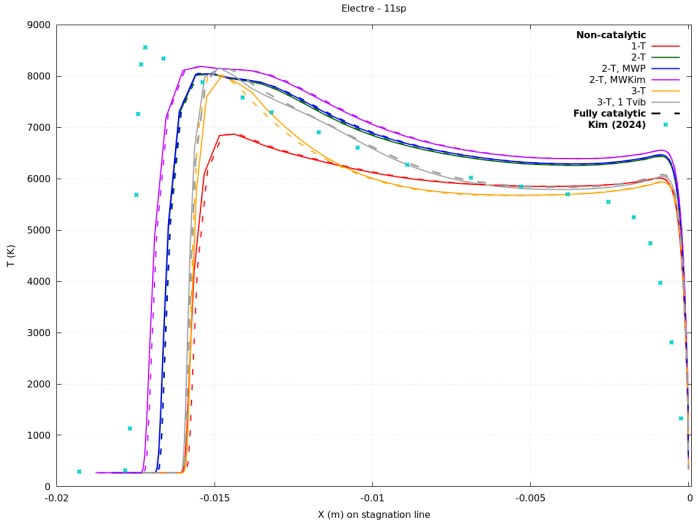

(a) Translational

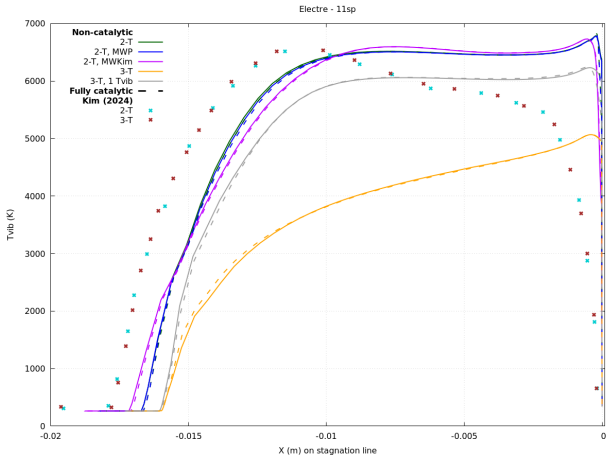

(b) Vibrational

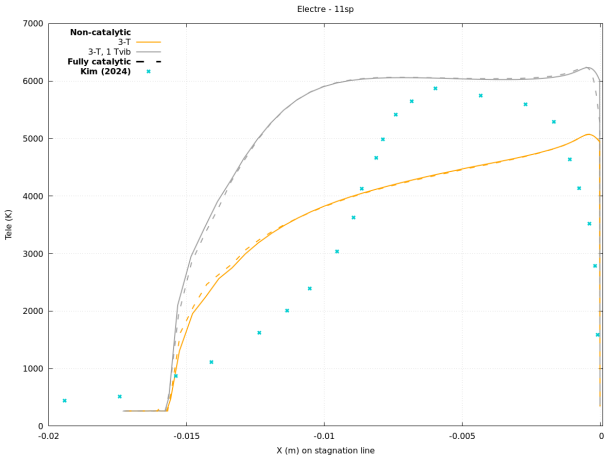

(c) Electron-electronic

Figure 6: Temperature profiles along the stagnation line

Larger discrepancies between models appear for the vibrational profiles in Figure 6b. The 2-T approaches (MWP and MWKim) exhibit rapid vibrational excitation and reach equilibrium with T relatively close to the shock front. In contrast, the 3-T model, which plots the vibrational temperature of N_2 for comparison as multiple vibrational temperatures are present and N_2 is the dominant species, shows a significantly slower rise. A variant of the 3-T model that assumes a single vibrational temperature yields results more consistent with the 2-T approaches. The fully catalytic wall condition leads to a slight reduction in vibrational heating, which is consistent with enhanced recombination of dissociated nitrogen atoms at the fully catalytic wall. Recombination reactions release energy primarily into translational modes or surface

heating rather than vibrational excitation. As a result, the overall demand for vibrational energy to support dissociation decreases, leading to a reduction in vibrational heating near the wall. Furthermore, the 2-T models reproduce the same steep rise and approach to equilibrium as observed by Kim [3], whereas the 3-T prediction tends to lag behind, particularly within the shock layer.

For the electron-electronic temperatures in Figure 6c, T_{ele} rises sharply through the shock, but with slightly lower values for the 3-T model. The non-catalytic and catalytic cases remain close, suggesting that electronic excitation is mainly governed by the shock-induced ionization rather than wall processes. For the electron-electronic mode, agreement with [3] is good in both magnitude but less so in profile shape.

Overall, the stagnation line profiles confirm that translational and electronic temperatures equilibrate rapidly after the shock, while vibrational excitation proceeds more slowly, especially when treated in a three-temperature framework.

4.3 Heat flux distribution along the capsule skin

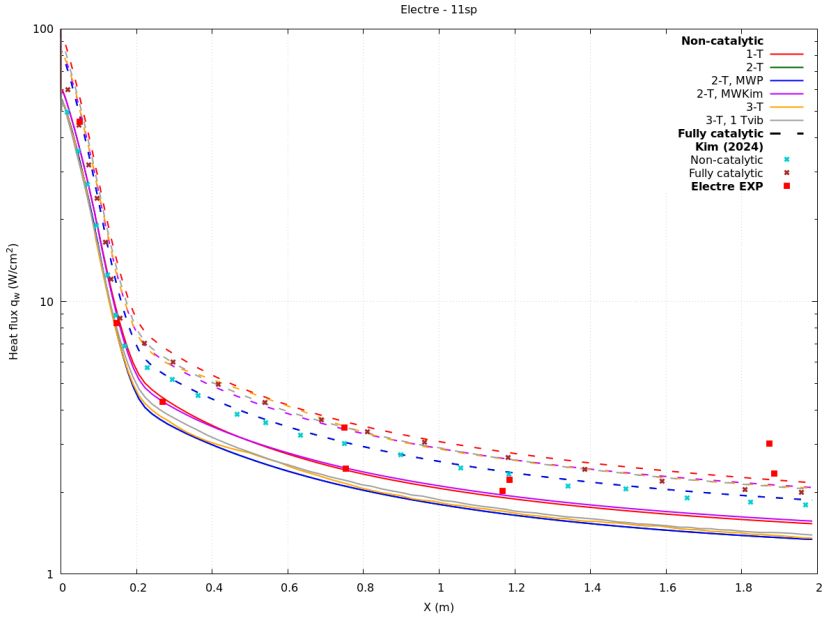

Figure 7: Wall heat flux profiles

The wall heat flux distribution is shown in Figure 7. All models capture the steep decrease in heat flux from the stagnation point towards the shoulder region. The magnitude at the stagnation point ranges between 80 and 100 W/cm^2 depending on the thermal model and catalyticity assumption.

Non-catalytic simulations consistently underpredict the experimental data (Electre EXP), while the fully catalytic cases systematically overpredict it, particularly near the stagnation

point. The partially catalytic reality is therefore expected to lie between these two limiting cases. The 2-T and 3-T models yield nearly indistinguishable heat flux profiles, indicating that wall heat transfer is less sensitive to the internal energy model than to the catalytic boundary condition.

Comparison with Kim [3] shows reasonable agreement in both trend and magnitude, further supporting the validity of the present simulations. However, discrepancies in the shoulder region highlight remaining uncertainties in both experimental data and surface chemistry modeling.

4.4 Electron number density normal to the wall

4.4.1 At 0°

Additionally, Figure 8 presents the electron number density along the stagnation streamline. A sharp rise in N_e is observed immediately downstream of the shock, followed by a gradual approach to a plateau towards the wall. The density spans nearly ten orders of magnitude, from 10^{10} to 10^{20} m^{-3}.

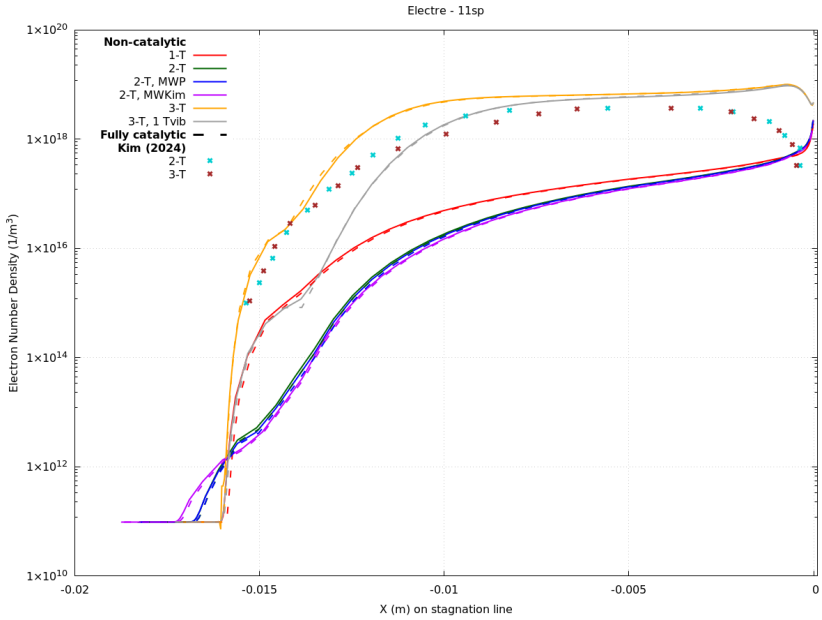

Figure 8: Electron number density profile along the stagnation line

The 1-T and 2-T models predict lower electron densities compared to the 3-T cases, which yield values closer to the reference results from [3]. In particular, the 3-T model captures both the sharp ionization front and the subsequent saturation level, whereas the simplified models tend to underpredict ionization rates.

The influence of wall catalyticity is barely visible: all models converge towards similar stagnation-point values. These trends confirm that a detailed multi-temperature treatment is essential to accurately capture ionization kinetics in high-enthalpy entry flows.

4.4.2 At 30° and 75°

Figure 9 compares the electron number density normal to the wall at the 30° and 75° position from the nose. When comparing NSMB results with Kim's data [3], the overall magnitudes are comparable, but the profiles appear stretched in space. This discrepancy suggests a potential factor-of-two scaling issue, possibly due to a radius-versus-diameter interpretation. While the exact source of this discrepancy remains unclear, this introduces an uncertainty in the comparison.

Figure 9 presents the corrected NSMB results, obtained by applying a scaling factor of 0.5 to the spatial coordinate.

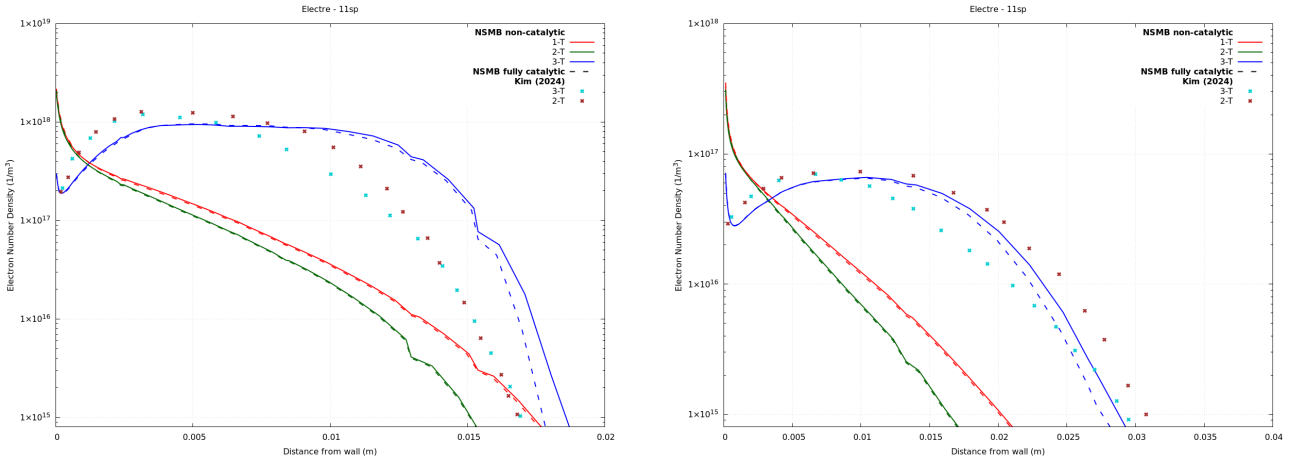

(a) At 30°

(b) At 75°

Figure 9: Electron number density profiles normal to the surface at different angular positions from the nose

The 1-T and 2-T models show noticeable deviations from the reference, both in profile shape and magnitude. In contrast, the 3-T model exhibits significantly better agreement with Kim's results [3], particularly at 75° (Figure 9b), where both the peak values and the profile shape align closely.

5 Conclusions

The numerical investigation of the ELECTRE reentry case demonstrates that thermo-chemical non-equilibrium modeling is essential for accurately simulating hypersonic flows. Using the NSMB solver and 11-species air models, simulations reproduced key physical behaviors observed in flight, particularly in terms of shock-layer structure and surface heat flux.

The results demonstrate that while translational and electronic temperatures equilibrate rapidly after the shock, vibrational energy modes require more detailed treatment to capture their slower excitation dynamics. Surface catalyticity strongly influences vibrational heating and heat flux predictions, underscoring the need for realistic boundary condition modeling. Moreover, multi-temperature approaches are essential for accurately resolving ionization processes in the shock layer.

These findings highlight the importance of advanced physical models and surface chemistry representations in simulating high-enthalpy atmospheric entry flows with fidelity.

References

[1] Hoarau Y., Pena D., Vos J. B., Charbonnier D., Gehri A., Braza M., Deloze T., Laurendeau E., *Recent developments of the Navier-Stokes Multi Block (NSMB) CFD solver*, AIAA SciTech 2016, 4–8 Jan, San Diego, CA. DOI: 10.2514/6.2016-2056

[2] Muylaert J., Walpot L., Hauser J., Sagnier P., Devezeaux D., Papirnyk O., Lourme D., *Standard Model Testing in the European High Enthalpy Facility F4 and Extrapolation to Flight*, AIAA 17th Aerospace Ground Testing Conference, 6–8 July 1992, Nashville, TN. DOI: 10.2514/6.1992-3905

[3] Kim C., Kim K. H., Yang Y., Kim J. G., *Effect of multi-temperature models on heat transfer and electron behavior in hypersonic flows*, *Physics of Fluids*, Vol. 36, 096127, 2024. DOI: 10.1063/5.0223900

[4] Kim J. G., Kang S. H., Park S. H., *Thermochemical nonequilibrium modeling of oxygen in hypersonic air flows*, *International Journal of Heat and Mass Transfer*, Vol. 144, 119059, 2019. DOI: 10.1016/j.ijheatmasstransfer.2019.119059

[5] Hao J., Wang J., Lee C., *Numerical study of hypersonic flows over reentry configurations with different chemical nonequilibrium models*, *Acta Astronautica*, 2016. DOI: 10.1016/j.actaastro.2016.04.014

[6] Li J., Pan H., Zhang L., Miao W., Chen Z., Cheng X., *Real Gas Effect on a Standard Model Electre*, APISAT2014 – 2014 Asia-Pacific International Symposium on Aerospace Technology, *Procedia Engineering*, 2015. DOI: 10.1016/j.proeng.2014.12.552

[7] Wang X. Y., Yan C., Zheng Y. K., Li E. L., *Assessment of chemical kinetic models on hypersonic flow heat transfer*, *International Journal of Heat and Mass Transfer*, 2017. DOI: 10.1016/j.ijheatmasstransfer.2017.03.102

[8] J. G. Kim and S. M. Jo, *Modification of chemical-kinetic parameters for 11-air species in reentry flows*, International Journal of Heat and Mass Transfer, vol. 173, 2021, Article 121221. DOI: 10.1016/j.ijheatmasstransfer.2021.121221